Performance analysis of
the METEOSAT Third Generation Infrared Sounder candidate mission.

Stephen Tjemkes, Jochen Grandell, Régis Borde, Rolf Stuhlmann
EUMETSAT, Am Kavalleriesand 31, D-64295 Darmstadt, Germany
contact:stephen.tjemkes@eumetsat.int

Introduction

To ensure continuity of the operational services, EUMETSAT is currently preparing for the third generation of the Meteosat geostationary satellite. Four candidate missions will be studied during the phase A activities, the High Resolution Fast Imagery (HRFI), the Full Disc High Spectral resolution Imagery (FDHSI) (which potentially will be implemented through a single instrument, namely the Flexible Combined Imager (FCI)), the Infrared Sounder (IRS) and the Lightning Imagery (LI) mission. The ESA-lead industrial part of the Phase A activities will start in 2007. The current paper considers the IRS candidate mission.

IRS candidate mission has the primary objective to support NWP at regional and global scales with information on atmospheric dynamics, notably the AMV in clear areas. A further primary objective is to provide high frequency information on thermodynamical structure of the atmosphere. A secondary objective is to support emerging operational air chemistry and air quality applications.

The first mission objective is based upon the experience with the derivation of Atmospheric Motion Vectors (AMV) derived from the displacement of cloudy targets from a time sequence of observations. Using observations in the two MSG-WV channels (MSG WV 6.2 and WV 7.3), it would theoretically be possible to derive these AMV using displacement of water vapour features, seen in clear sky area's. However, the complex vertical distribution of moisture together with the relatively deep atmospheric layers observed, prevents an accurate height assignment of these tracked features. This limits the usefulness these clear sky AMV's.

As demonstrated by AIRS, hyperspectral observations can be used to accurately depict $q(z)$ and this would solve the height assignment problem. Hence, to derive AMV using clear sky targets from hyperspectral observations by IRS the following steps are required:

- retrieve $q(z)$ from IRS observations, and

- perform a feature tracking at a particular level (e.g. 850 hPa) from a sequence of product images.

As an illustration of the basic idea to use displacement of moisture features to infer information on the atmospheric dynamics consider Fig. 1. In this Fig. the specific humidity at approximately 400 hPa taken from a model simulation of the observations collected during Bow-Echo and Mesoscale Convective Vortex Experiment (BAMEX) at 10 June 2003. Shown are the simulations at 17:00 and 17:20 UTC. A more complete discussion of the adopted test data is given below. From these two modeled moisture fields the displacement vector at this level can be calculated and this is shown in the left

panel of Fig. 2. A visual comparison with the simulated wind vector at 400 hPa shows the large degree of commonalities between the displacement vectors and the wind field, though several differences between the two panels are easy to detect as well.
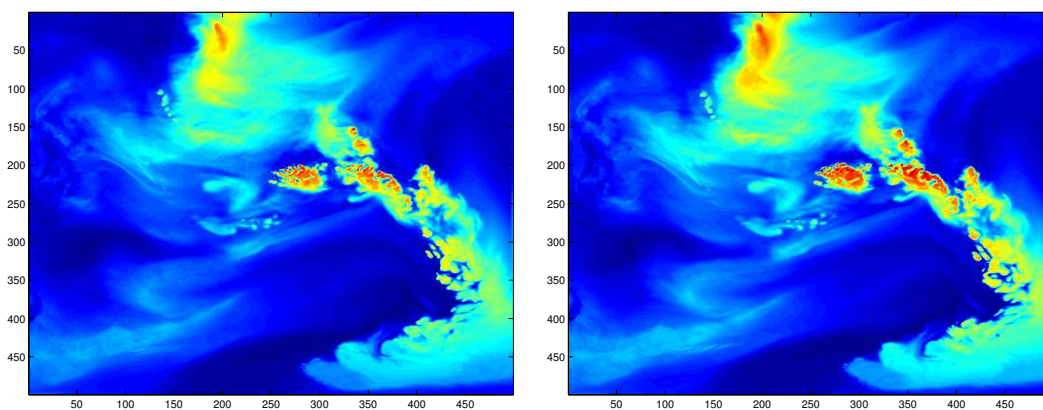

Figure 1 Horizontal distribution of specific humidity at 400 hPa according to a model simulation by the WRF model for the Bow-Echo and Mesoscale Convective Vortex Experiment (BAMEX). Shown are the specific humidity at 17:00 UTC (left panel) and 17:20 UTC (right panel) on 10 June 2003.
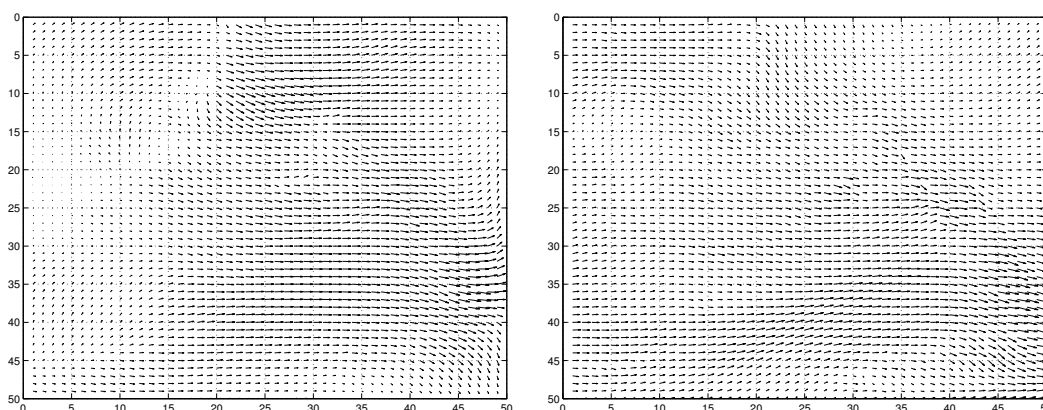

Figure 2 Left panel: displacement vectors calculated from the the displacement of specific humidity fields shown in Fig. 1, right panel the modeled wind vectors at 17:00 UTC on 10 June 2003. Note that for readability not all vectors are shown. Presented are the vectors for every 10th pixel of Fig. 1.

The objective of the current work is to document the capabilities of the IRS candidate mission to meet its mission objective. To do this a mandatory step is to demonstrate the capabilities to accurately depict q(z). This is done through an information content analysis and a retrieval simulation. Thereafter, an initial analysis of the sensitivity of clear sky AMV to IRS characteristics will be presented as well.

Band	Domain [cm⁻¹]	Domain [μm]
LWIR	$700 - 1210$	$8{,}26 - 14{,}29$
MWIR	$1600 - 2175$	$4{,}60 - 6{,}25$

Table 1 IRS Specifications
according MRD 2

MTG IRS

For the current analysis the latest IRS specifications decided by the MTG Mission Team (MMT) were adopted (MRD, V2 available from www.eumetsat.int). A summary of these specification is listed here. The MMT decided that, as a baseline, the IRS should be a Fourier Transformation Spectrometer (FTS) system with a Maximum Optical Path (MOPD) of 0.8 cm. This would correspond to a spectral sampling $\delta\nu$ of 0.625 cm^{-1} as $\delta\nu = 1.0/(2.0 * MOPD)$. Furthermore, the IRS should cover the two spectral bands indicated in Table 1, and a radiometric noise specification as illustrated in Fig. 3. As a goal the IRS should scan the full disc in 30 min with a threshold of 60 min.
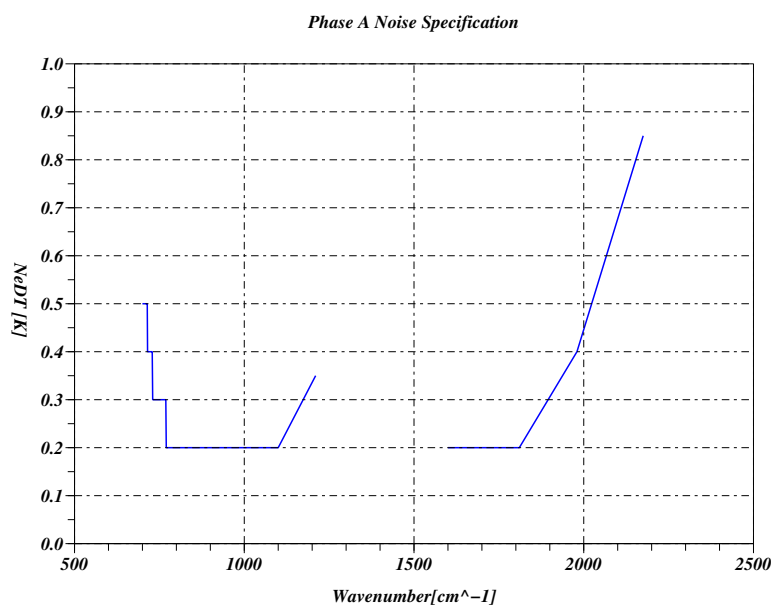
Phase A Noise Specification

Figure 3 Radiometric performance according MRD 2.

Information Content

In this section the performance of the IRS candidate mission to depict vertical moisture profile is analysed using the theoretical information content framework prepared by

Rodgers (2000). First a brief outline of the method is presented followed by a discussion of the results.

Theoretical Framework

Assume that atmospheric states can be expressed as a probability density function, with Gaussian error statistics. Furthermore, assume there is prior knowledge of these states (x_a) before a measurement is made. Finally a linear relation between a measurement (y) and the real state vector (x):

$$y = \mathbf{K}x + \epsilon, \tag{1}$$

where ϵ represents the measurement error and $\mathbf{K}$ the Jacobians (the change of the radiance as a function of state) is adopted.

With these assumptions, a new state $\hat{x}$ can be derived under the condition of minimal posterior error covariance.

$$\hat{x} = x_a + \mathbf{G}\left(y - \mathbf{K}x_a\right), \tag{2}$$

with corresponding error covariance matrix

$$\mathbf{S}_{\hat{x}} = \mathbf{S}_a - \mathbf{S}_a\mathbf{K}^T\left(\mathbf{K}\mathbf{S}_a^{-1}\mathbf{K}^T + \mathbf{S}_y^{-1}\right)^{-1}\mathbf{K}\mathbf{S}_a,$$

the Gain function ($\mathbf{G}$) follows from:

$$\mathbf{G} = \left(\mathbf{K}^T\mathbf{S}_y^{-1}\mathbf{K} + \mathbf{S}_a^{-1}\right)^{-1}\mathbf{K}^T\mathbf{S}_y^{-1}. \tag{3}$$

To demonstrate the capabilities of an instrument to depict the state, the degrees of freedom for signal (DOFS) are used which can be calculated from the above using the so-called Averaging Kernel. Rewriting eq. 2 using the linear relation between the observations y and the true state x (eq. 1), we find

$$\hat{x} = \left(\mathbf{I} - \mathbf{A}\right)x_a + \mathbf{A}x + \mathbf{G}\epsilon \tag{4}$$

where the averaging kernel $\mathbf{A} = \mathbf{GK}$ follows from:

$$\mathbf{A} = \mathbf{I} - \mathbf{S}_{\hat{x}}\mathbf{S}_a^{-1}.$$

Then the DOFS is defined by (Rodgers, 2000):

$$D = trace\left(\mathbf{A}\right).$$

Note that eq. 4, expresses the retrieved state as a linear combination of the a-priori and the true state.

Given a true state x and the corresponding error covariance of the state, it is possible to analyse the potential impact of the IRS observations to reduce the rms of the state as expressed by the DOFS. As this is a scalar quantity, this analysis can be done in a systematic way. Note that no explicit retrievals are required. However, the analysis potentially gives a too favourable result.

The posterior error covariance matrix is composed of the following elements (Rodgers, 2000):

- The *smoothing error* ($\mathbf{S}_s$):

$$\mathbf{S}_s = (\mathbf{A} - \mathbf{I}) \, \mathbf{S_x} \, (\mathbf{A} - \mathbf{I})^T, \tag{5}$$

- the *retrieval noise error* ($\mathbf{S}_m$):

$$\mathbf{S}_m = \mathbf{G S_y G}^T. \tag{6}$$

Other components identified by Rodgers (2000) are not considered here, such that the posterior error covariance matrix can be written as:

$$\mathbf{S}_{\hat{x}} = \mathbf{S}_s + \mathbf{S}_m. \tag{7}$$

Setup of the analysis

From the above, the performance analysis of the IRS requires an atmospheric state, an associated error covariance matrix and Jacobians. To characterise the atmospheric state the 80 diverse profiles extracted from the ERA-40 dataset (so-called SDr dataset from the SD-60L dataset prepared by Chevallier (2002) was adopted. The error covariance matrix from the ECMWF short range weather forecast model was provided by J.N. Thepault and A. Collard (private comm.). The Jacobians for temperature and atmospheric constituents have been calculated by a LBLRTM (Clough et al., 2004), which is a state of the art line-by-line model, currently capable to calculate these Jacobians analytically. Instrument specification according to MRD V2, which are baseline for Phase A - activities.
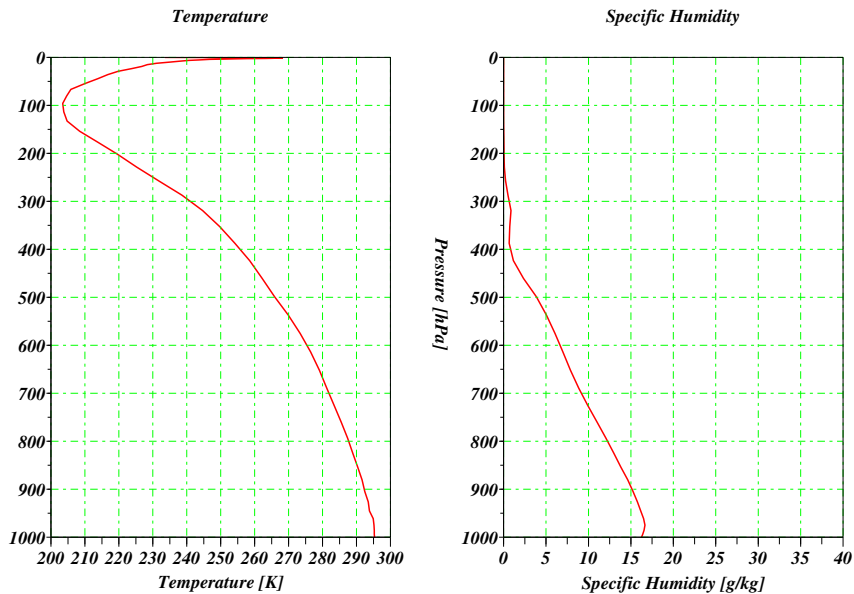

Figure 4 Thermodynamical Profile

Results of Analysis

The DOFS calculated when the two IRS bands (MWIR and LWIR respectively) are considered in synergy and when used separately for the profile shown in Fig. 4 are listed in Table 2.

Domain	Humidity	Temperature
MWIR	6.0	1.7
LWIR	3.7	2.0
LWIR and MWIR	6.5	3.2

Table 2 Degrees of Freedom for moisture and temperature for the profile shown in Fig. 4

For this profile results indicate that for moisture DOFS calculated for the MWIR alone is larger than for the LWIR, while for temperature the opposite is true. Furthermore when both bands are analysed in synergy the DOFS for the combination is larger than for the individual bands, but no linear dependency. Finally the DOFS for moisture is significantly larger than for temperature, which might be a reflection of the relatively high quality of the ECMWF temperature information.
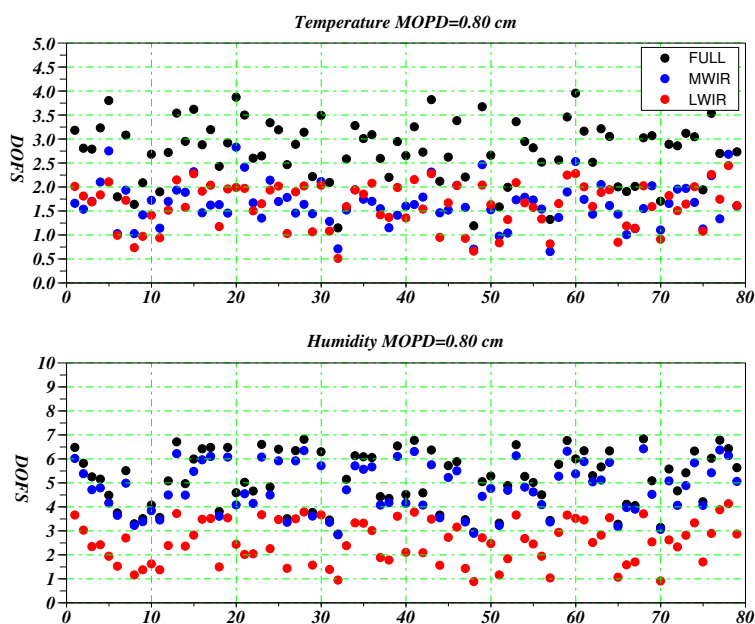

Figure 5 DOFS for temperature (top panel) and moisture (bottom panel) for 80 divers profiles of Chevallier dataset when the MWIR, LWIR bands are analysed separately (blue and red dots respectively) and when both bands are analysed in synergy (black dots).

The value of the DOFS depends on the actual profile as seen from Fig. 5 were the DOFS for all 80 profiles of the SDr-dataset are presented. From this it can be seen that the values

presented in Table 2 are a little bit high for moisture but very typical for temperature. Important to realise is that although temperature and humidity can be inferred from each band separately, the results suggests the importance of considering both bands in synergy to infer the temperature and to a lesser degree the moisture structure of the atmosphere.

Averaging Kernel

DOFS gives only bulk information, to see where this information originates from we can look at the Averaging Kernel. Recall eq. 4 which indicates that the retrieved state is a linear combination of the a-priori and the true state:

$$\hat{x} = (\mathbf{I} - \mathbf{A}) \, x_a + \mathbf{A} x + \mathbf{G} \epsilon, \tag{8}$$

with $\mathbf{A} = \mathbf{GK}$ the so-called averaging kernel. Hence we see that the Averaging Kernel weights the contribution of the true state to the retrieval state. Ideally $\mathbf{A} = \mathbf{I}$, then the retrieved state is the actual state "blurred" by radiometric noise, which is projected onto the state by the Gain function (i.e. the last term in eq. 8). However, the Averaging Kernel calculated for the profile shown in Fig. 4, looks quite different as shown in Fig. 6.
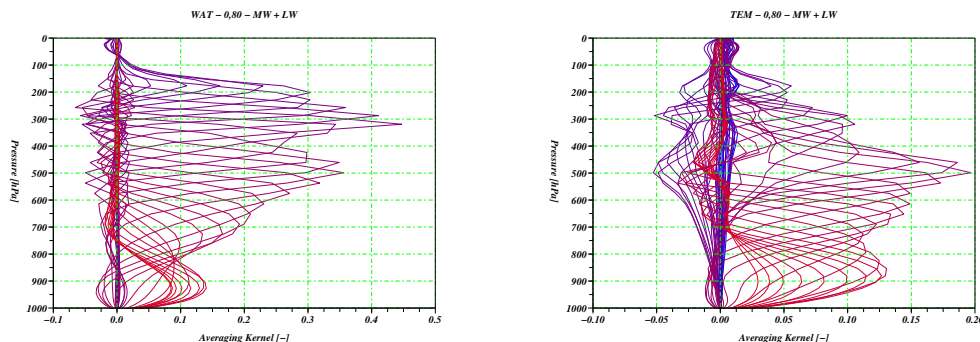

Figure 6 Averaging Kernel for moisture (left panel), and temperature (right panel). Colors indicate the different columns of the averaging kernel matrix. The averaging kernel is calculated for the profile shown in Fig. 4 and when both IRS spectral bands are considered in synergy.

The figures for the averaging kernel indicate that the contribution to the retrieval state by the actual state is significantly smoothed. This will limit the capabilities to retrieve small scale structures from the IRS.

Error budget

The variance components of the prior and posterior error covariance shown in Fig. 7, shows that for moisture and temperature the observations reduce the prior variance throughout the entire troposphere. Also seen is that the reduction of the temperature variance is less than that of moisture. The IRS observations reduce the temperature variance for layers
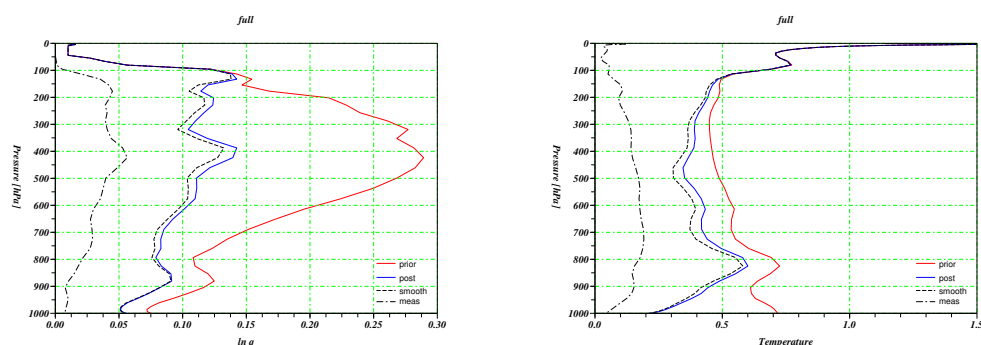
Figure 7   Variation of the prior and posterior moisture variance for the profile shown in Fig. 4 with pressure. Red line represents the prior and blue line the posterior moisture variance. Also shown the corresponding smoothing (dashed black line) and measurement (dashed dot black line) error contribution to the posterior error variance.

near surface, which is largely due to correlations in the prior error covariance matrix as shown in the next section.

The break down of the posterior error according to eq. 7, indicates that the smoothing error dominates the budget and that the contribution by the measurement error is relatively small. This suggests that the measurement error is reduced by making optimal use of the large number of similar but independent observations by the different channels of the IRS. As will be discussed later, results of the retrieval simulations do not show the same independence to the radiometric performance of the candidate instrument.

Selected sensitivity results

To illustrate the sensitivity of the results to different settings of selected parameters some results are presented here. Table 3 shows the sensitivity of the DOFS by changing the MOPD. Three different MOPD values are considered, namely 0.4, 0.8 (baseline) and 1.0 cm respectively.

The Table shows that indeed the DOFS depends on the MOPD value. The larger the MOPD, the higher the DOFS, though there appears to be no linear dependency. It can further be noticed that the increase of the DOFS for temperature is larger than for moisture, especially when both bands are analysed in synergy.

Fig 8 shows the corresponding variation of the posterior variance for moisture and temperature with height for the three MOPD values. These results indicate that near the surface the posterior variance is insensitive to the value of the MOPD. There appears to be some sensitivity in the middle and upper troposphere, but only when the MOPD is increased from 0.4 to 0.8 cm. There appears little advantage to increase the MOPD from 0.8 to 1.0 cm.

Domain	MOPD (cm)	q	T
MWIR	0.40	5.4	1.2
	0.80	6.0	1.7
	1.00	6.2	1.8
LWIR	0.40	3.1	1.3
	0.80	3.7	2.0
	1.00	3.8	2.2
LWIR and MWIR	0.40	5.9	2.2
	0.80	6.5	3.2
	1.00	6.7	3.5

Table 3 Degrees of Freedom for moisture and temperature for the profile shown in Fig. 4, as a function of MOPD
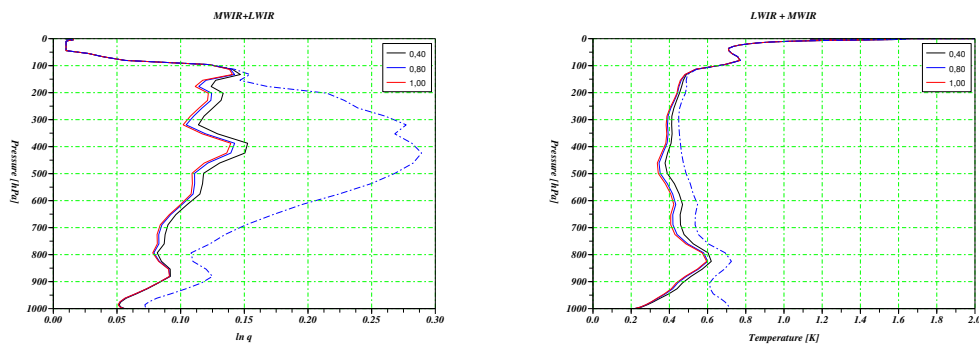

Figure 8 The variation of the posterior error variance of moisture (left panel) and temperature (right panel) with pressure for three values of the MOPD, 0.40 (solid black), 0.80 (solid blue) and 1.0 (solid red) cm. Also shown is the prior error variance as a dashed blue line.

Diagonal prior error covariance

To illustrate the effects of correlations between layers in the prior error covariance matrix, the error budget of the posterior error co-variance matrix was calculated using a modified prior error covariance matrix. For these simulations we used the variance of the ECMWF prior error co-variance, but set all off-diagonal elements to zero. This prevents correlation between the different layers. The results shown in Fig. 9 indicate that if these correlations in the prior error covariance matrix are not taken into account, the reduction of errors is significantly reduced. There is some reduction of the moisture variance in the middle troposphere, but there is hardly any reduction of the temperature variance.
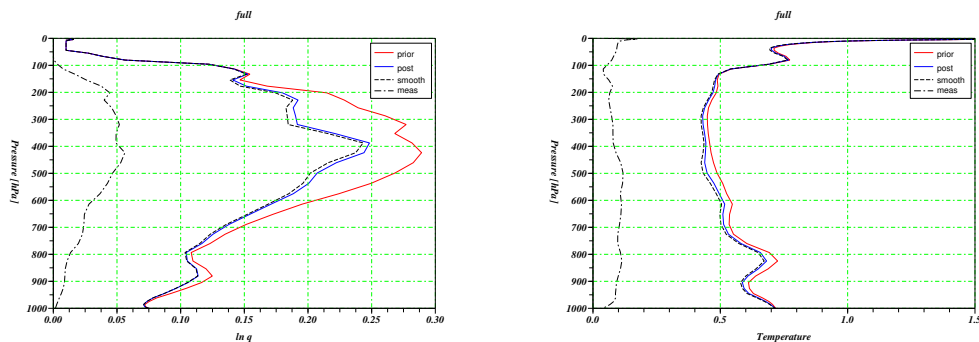
Figure 9   Same as Fig. 7, but now when the off-diagonal elements of the prior error covariance matrix are set to zero.

Sensitivity analysis of scene inhomogeneity

The above discussion assumed that the observation is taken over a homogeneous scene. In reality different effects will render the scene inhomogeneous. For instance due to diffraction, radiation from nearby clouds could "leak" into the cloud-free scene and can cause a degradation of the observation. This degradation is often called pseudo-noise, although it might have more a systematic behaviour than a random. Using AIRS observations the magnitude of the pseudo-noise has been estimated for different fields as shown in Fig. 10. It is important to note that the Figs. does not show the absolute value of the pseudo noise, but the value relative to the pseudo noise at 1600 cm−1. Though the precise magnitude and dependency of the pseudo-noise with wavenumber depends on the particular scene, what can be seen is that the pseudo noise has its largest values in the long wavelength parts of the spectrum. The pseudo noise shown in Fig. 10 can potentially result in a bias of the retrieved state parameters. Using linear analysis the bias in the state vector (Δx) is related to the bias in the measurement (Δy) through:

$$\Delta \hat{x} = \mathbf{G} \Delta y, \tag{9}$$

where $\mathbf{G}$ is the Gain function defined by eq. 3.

AIRS does not make observations in the IRS-MWIR spectral domain. Pending availability of IASI observations, we assume that the AIRS observations in the spectral domain between 1200 and 1600 cm^{-1} are also representative for the observations in the 1600 - 2000 cm^{-1}. For our analysis we mirrored the derived pseudo-noise from the 1200–1600 cm^{-1} domain into the 1600 - 2000 cm^{-1} domain.

From linear mapping of the pseudo-noise as shown in Fig. 11, a relatively large bias in temperature and moisture is found for the broken cloud situation. Smaller biases are found for the other scenes, but they are not negligible. The bias in the moisture for the broken cloud, and atlantic low pressure situation, is surprisingly large, given the magnitude of the the pseudo-noise in the water vapour band. Apparently the large values of the pseudo-noise in the edges of the 14 micron band, dominates the signal.

As discussed above, the DOFS for moisture for the MWIR band alone is about the same as the DOFS when MWIR and LWIR are analysed together (cf. Fig. 5). Hence for
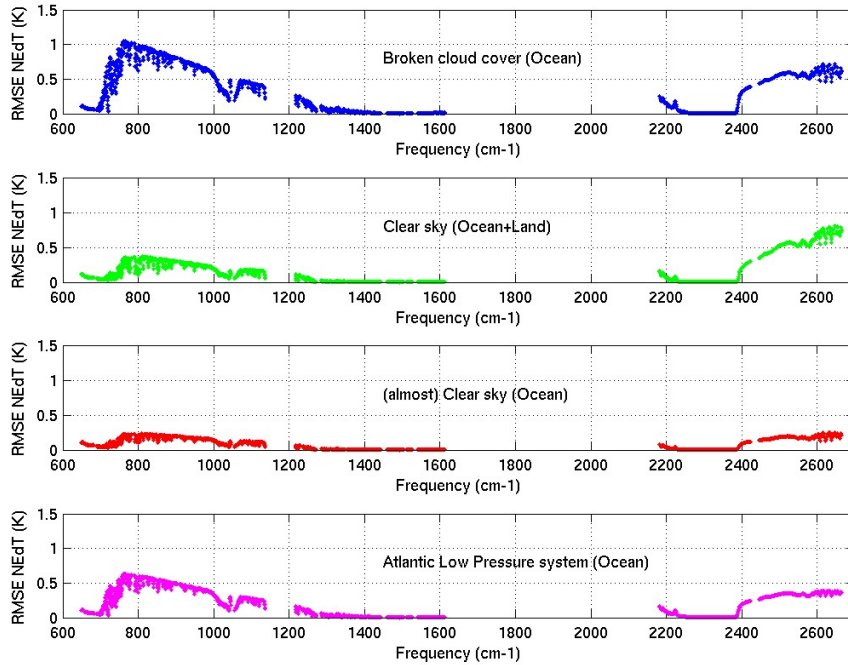
Figure 10 Pseudo-noise as function of wavenumber derived from AIRS observations over different geographical areas. Note that the pseudo-noise has a negative value.
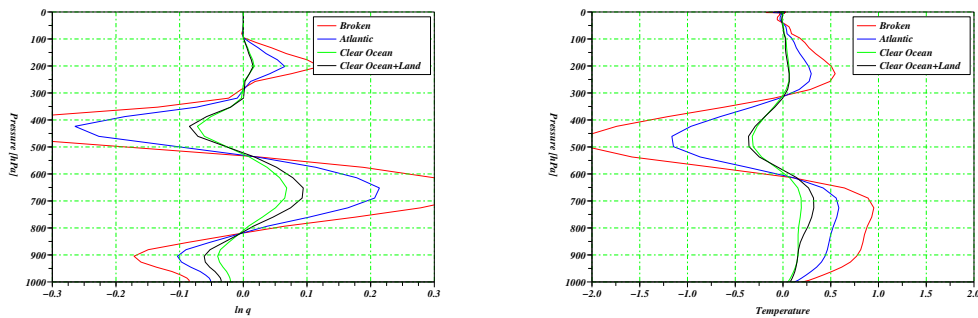

Figure 11 Lineair mapping of the pseudo-noise shown in Fig. 10 onto the state vectors.

moisture one could consider a moisture retrieval using the MWIR band alone, and thus avoid the pseudo-noise induced bias. For temperature this could also be done, although Fig. 5) suggests there will be some performance loss, i.e. the posterior error will be larger in case the MWIR alone is used in the retrieval compared to the retrievals when both LWIR and MWIR are used in synergy. This is confirmed in Fig. 12 where the posterior temperature and moisture variance are shown when only the observations in the MWIR

band are considered. These results should be compared to the situation presented in Fig. 12 where both bands (LWIR and MWIR) are considered. And this comparison shows that especially the posterior temperature variance for the mid and upper tropospheric layers is considerable smaller in Fig. 7 than in Fig. 12 as expected.
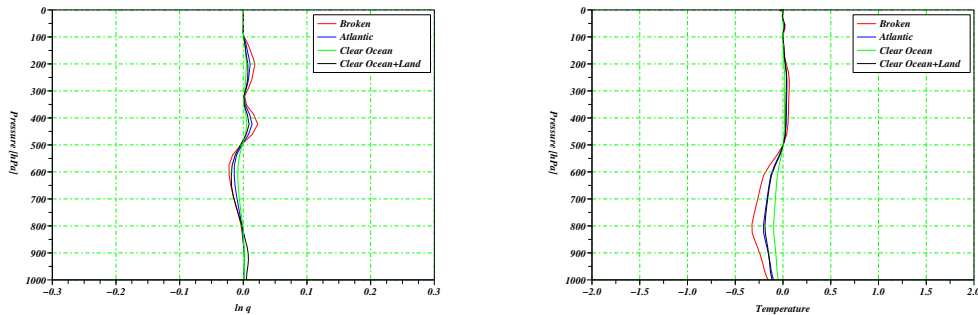

Figure 12 Lineair mapping of the pseudo-noise shown in Fig. 10 onto the state vectors, when only the MWIR band is used.
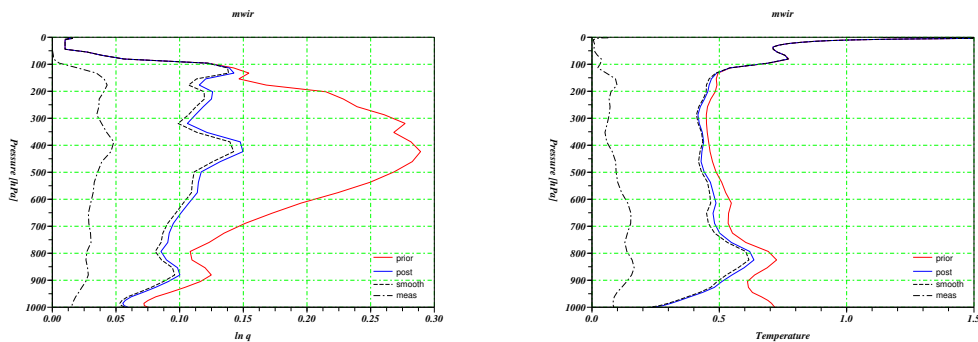

Figure 13 Variation of the prior and posterior moisture variance for the profile shown in Fig. 4 with pressure when only the information from the MWIR band are used. Blue line represents the prior and red line the posterior moisture variance. Also shown the corresponding smoothing (dashed black line) and measurement (dashed dot black line) error contribution to the posterior error variance.

The magnitude of the pseudo-noise induced bias will depend on the actual situation, i.e. the proximity of the clouds to the cloud free pixel, the cloud type etc. And a more quantitative analysis will be a future study subject. Despite this, the initial results of this analysis shows the importance of a proper characterisation of the domain from which the observations are extracted. Unless an explicit treatment for the bias due to nearby clouds in the observations is provided, observations of cloud free pixels, when clouds are in the vicinity (say 2-5 pixels away) should be treated with great care. This could strongly limit the capabilities of an IRS in geo-orbit to monitor thermodynamical profiles in regions dominated by clouds ("whole hunting" in the storm track region).

It is important to realise that the observations in the LWIR channel are important for other applications than the retrieval of temperature and humidity profiles. For instance they can be used to detect clouds and to correlate the IRS observations with the observations by the FCI. The effects of the pseudo-noise on applications beyond the retrieval of temperature and humidity profiles is beyond the scope of the current paper.

Retrieval Simulation Experiment

For the information content analysis no explicit retrievals are required. This could lead to a too favourable results. Here performance of the MTG-IRS is demonstrated with the aid of a retrieval simulation. Objective is to use demonstrate the capabilities of the IRS to retrieve the vertical profile of moisture and temperature. Furthermore, the time evolution of the horizontal distribution of the retrieved moisture field is used to derive atmospheric motion vectors (AMV).

The (q,T) retrieval package adopted for the present studies is the Empirical Orthogonal Function (EOF) retrieval described by Li *et al.* (2000) and the code to generate the AMV is an optical flow (OF) method described by Corpetti *el al.* (2002), Horn and Schunck (1981) Szantai and Désalmand (2004), Zhou *et al.* (2000). Both the EOF retrieval and the OF are briefly described here.

Statistical retrieval of humidity and temperature

The EOF retrieval packages consists of a radiative transfer model, an EOF decomposition module, a linear regression module, and the actual EOF-retrieval.

Radiative Transfer The radiative transfer model generates the synthetic radiance at top of atmosphere for a given state vector. The state vector is taken from a database which is described below. The RTM generates a complete spectrum with spectral resolution according to an FTS system with an MOPD of 0.8 cm. This radiance dataset is decomposed using an Emperical Orthogonal Function (EOF) analysis, of which only the first 100 functions are maintained.

Statistical Retrieval: Training

The regression coefficients of the statistical retrieval are calculated from a training dataset. This is a sub-set of the entire radiance dataset. For each spectrum of the training dataset, the EOF scores are calculated for the truncated eigenvector set corresponding to the first 100 largest eigenvalues obtained from the EOF decomposition. Then regression coefficients are calculated using these EOF-scores and the state vector.

Statistical Retrieval: Validation

The spectra not used in the training dataset are used to validate or demonstrate the accuracy of the regression coefficients. For each spectrum of this so-called validation dataset the EOF-scores are calculated using the truncated eigenvector dataset. Then these scores are multiplied with the regression coefficients generated from the previous step and yield the retrieved state vector. From a comparison with the state vector used to generate the spectrum at top of atmosphere the accuracy of the retrieval method can be demonstrated.

Dataset

As indicated above, there are two dataset involved, one which is used to derive the regression coefficients from (the so-called training dataset) and one which is used to apply the coefficients to in order to retrieve the state vector (the validation dataset). These two dataset should be statistically independent.

For the retrieval simulation a different dataset than for the information content analysis was used. For our retrieval analysis results of a numerical simulation of severe convection observed during the Bow-Echo and Mesoscale Convective Vortex Experiment (BAMEX, Davis et al., 2004) by a Weather Research and Forecasting (WRF) model (Michalakes et al. 2001) were adopted. The simulations were done to provide guidance as to the optimal repeat cycle of water vapour convergence observations for now casting severe weather by the candidate imagery missions for the Meteosat Third Generation (Huang et al, 2005). The domain of the simulations consists of 500×500 grid points with a 4km horizontal grid spacing. A simulation of more than a complete diurnal cycle was performed (approximately 30 hours) with a time step of 20 minutes. The simulations captured the pre-convective environment, convection initiation and the subsequent mesoscale convection organisation of a number of severe convective cloud systems. Considered here are the simulations for June 10, 2003 00:00 UTC until June 11, 2003 02:20 UTC.

For the current simulations, profiles of temperature, moisture and the u,v components of the wind field are used. Though the model also calculated liquid and ice water content of clouds, these parameters were not considered here.

Optical Flow

In the present paper, the performance of the MTG-IRS candidate mission is demonstrated not only from an analysis of the accuracy of the retrieved vertical profile of q and T but also from an analysis of the time evolution of the horizontal distribution of q at a particular level, especially in relation to the capabilites to derive AMV from this evolution. To generate these AMV from the displacement of the features in the q-field the optical flow estimation of the wind field is used.

Optical-flow estimation aims at recovering the apparent displacement field between two consecutive frames in an image sequence. Such method has been considered in the context of fluid imagery either for satellite meteorological images in several recent works (Zhou *et al.*, 2000, Corpetti *et al.*, 2002, Szantai and Désalmand, 2004). In the original formulation Horn and Schunck, (1981) defined a functional $H = H_1 + \alpha H_2$ that needs to be minimised over the whole image. The first term H_1, so-called optical flow constraint (OFC), assumes the constancy of the luminance of a point along its trajectory. The second term H_2 of the functional H is usually a standard first-order spatial smoothness term. The coefficient α is tuned to increase or decrease the influence of the smoothness constraint on the vector calculation. Several variations of this initial principle have been successfully applied to various application domains in order to estimate deformation fields or motion fields. To capture specificities of image sequences with fluid motion, Corpetti *et al.* (2002) have modified the original relation based on the conservation of luminance, by the fluid law of mass conservation, also known as continuity equation. The term H1 of the functional H

now involves the divergence of the (horizontal) motion vector, and the regularisation term H_2 now includes both the divergence and curl (rotational) of the motion vector instead of the horizontal components (u, v) of the motion vector. A multi resolution procedure, which calculates the motion at different scales, is also applied in order to enable the determination of large vectors.
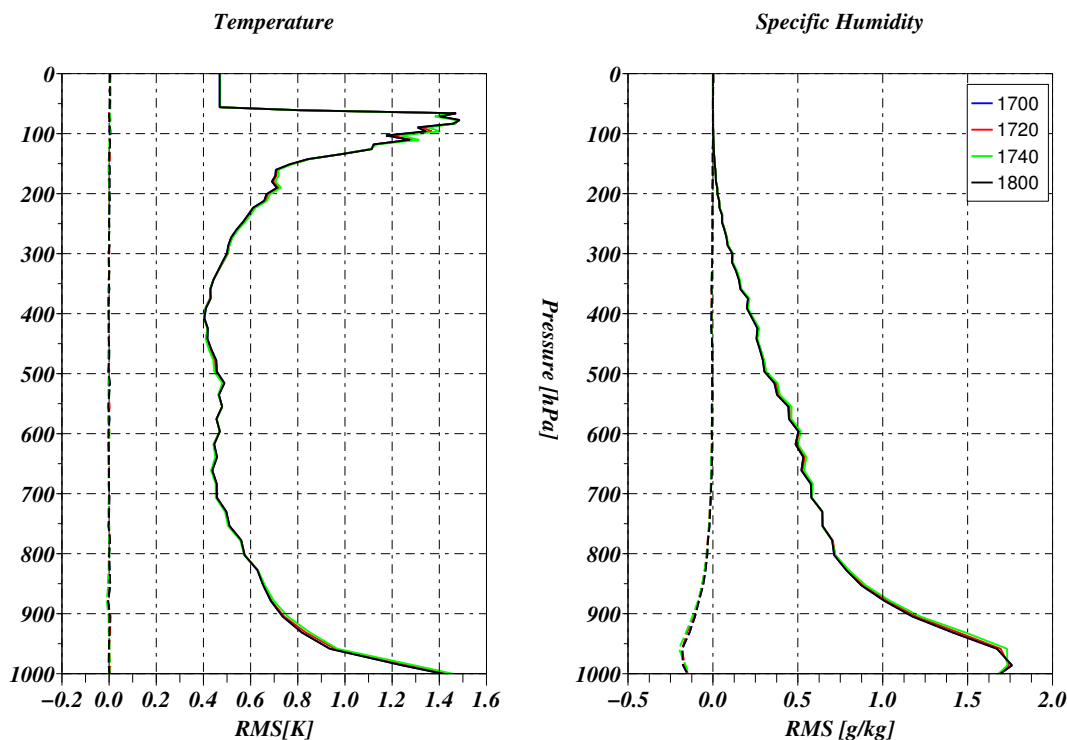
First Experiment

Figure 14 Variation of mean (dashed line) and variance (solid line) of the retrieved temperature (left panel) and specific humidity (right panel) for four different simulation times indicated by the colour coding presented in the legend.

In this experiment, the training and validation dataset were extracted from the same simulation time. To ensure independence of the training and validation dataset, 90% of the complete dataset was used for training and the remaining 10% for validation. For these simulations, both bands of the IRS were used, as well as the noise according to the MRD V2 specifications. Results for the four different simulation times are shown in Fig. 14. The mean difference between the retrieved and the original humidity and temperature profile is shown by the dashed lines while the standard deviation is shown by the solid lines. The color coding is according to the legend. That no color lines, besides the black are visible, indicates that the retrieval performance is not dependant on simulation time.

For temperature the variance of the retrieved profile is well below 0.5K in large parts of the troposphere. Near the surface the retrieved temperature increases to about 1.5 K. For specific humidity the variance is largely independent of the adopted dataset. It decreases rapidly from 1.2 g/kg at the surface to around 0 at 100 hPa.

Experiment 2

The first experiment demonstrates the general performance of the statistical retrieval to retrieve the vertical profile of temperature and specific humidity. In the second experiment the capabilities to retrieve the horizontal distribution of specific humidity is demonstrated. For this experiment the training was done using the simulation for 00:00 UTC, while the verification was done using the entire dataset for the subsequent time steps. This assumes that the distribution of temperature and humidity for 00:00 UTC will be representative for the other times, which is not the case. This will result in some performance degradation for the extreme temperature and humidity values, which will be localised to certain areas. However, it will not affect the general horizontal pattern of moisture.
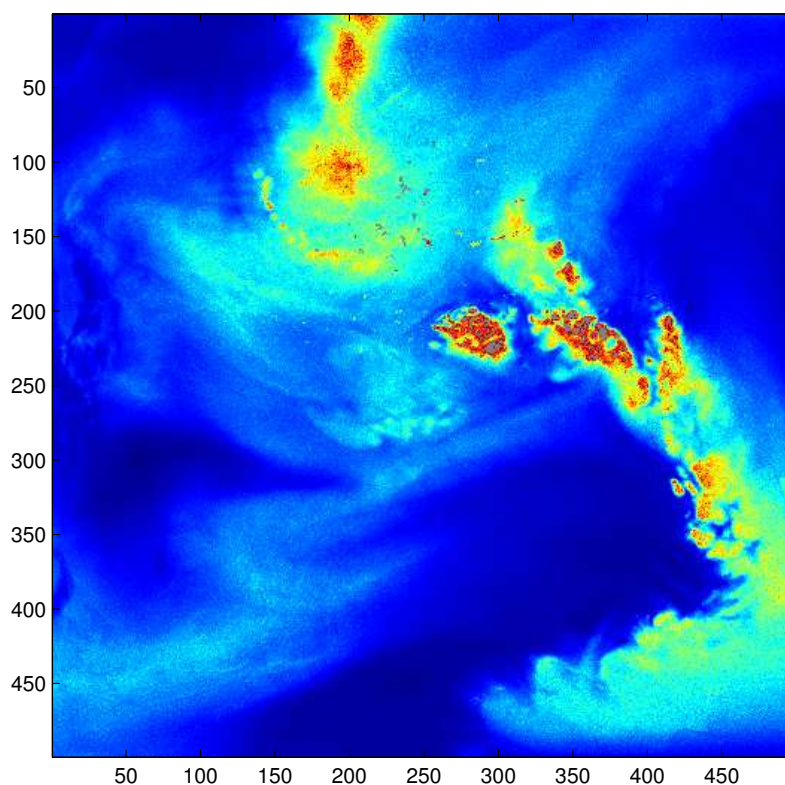

Figure 15 Geographical distribution of specific humidity at 17:20 UTC retrieved from the synthetic radiances calculated from the WRF model simulation for BAMEX observations on 10 june 2003
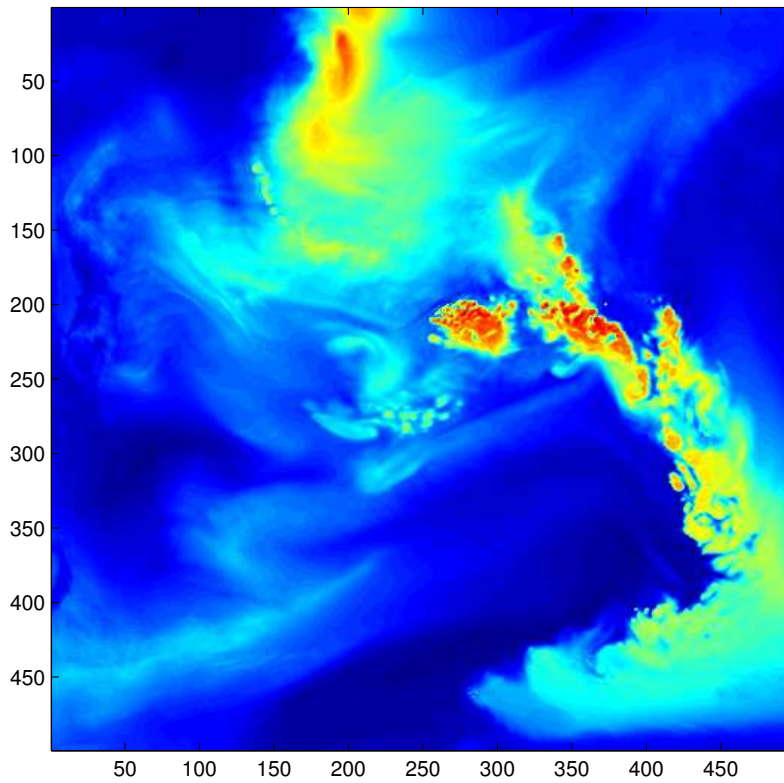
Figure 16 Geographical distribution of specific humidity at 17:20 UTC according to the WRF model simulation for BAMEX observations on 10 June 2003.

As an example Fig. 15 shows the the horizontal distribution of the retrieved specific humidity at 400 hPa for 17:20 UTC, which can be compared to the specific humidity at this level as simulated by the WRF model for this time shown in Fig. 16.

There appears to be large degree of communalities between the two figures. As expected the retrieved results appears to be more smooth that the reference. This is because any retrieval methods based on lineair regression tends to reduce variability. Furthermore, the radiometric noise tends to mask small scale variability further.

To demonstrate the smoothness of the retrieved humidity field a simple Fourier analysis was performed. A Hann data window was used to avoid features in the periodogram induced by the finite extend of the data record. Results are shown in Fig. 17, where the solid line represents the periodogram for the retrieved moisture field, and the dashed line indicates the results for the modeled, i.e. reference moisture field.

What can be seen from Fig. 17, is that in comparison to the the reference field, the retrieved moisture field has more energy at the smaller scales. In fact the periodogram for the retrieved moisture field at the smaller scales resembles almost a white noise spectrum. To demonstrate the performance for the entire time domain, the time evolution of the anomaly correlation coefficient is used. The anomaly correlation coefficient is defined as
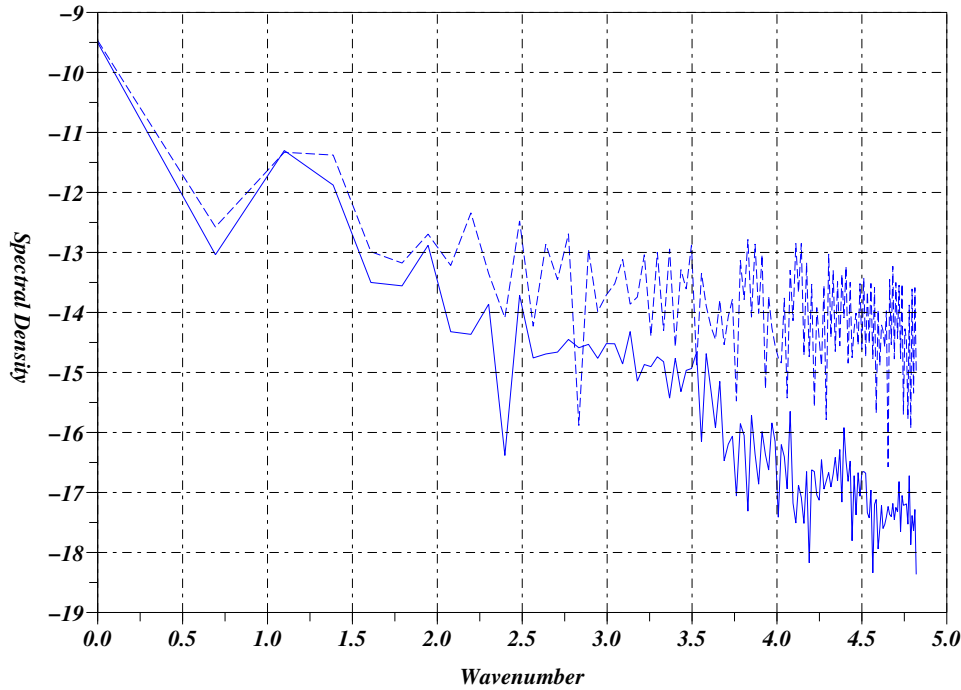
Figure 17 Periodogram of the specific humidity at 400 hPa. The solid line represents the periodogram derived from the true specific humidity while the dashed is the result for the retrieved values. Shown are the results for the 17:20 UTC dataset.

$$AC(t) = \frac{\sum \left[X(t) - \overline{\mathrm{X}}(t)\right]\left[X_r(t) - \overline{\mathrm{X}}_r(t)\right]}{\sqrt{\sum \left[X(t) - \overline{\mathrm{X}}(t)\right]^2 \sum \left[X_r(t) - \overline{\mathrm{X}}_r(t)\right]^2}}. \tag{10}$$

Here X represents the retrieved state variable (e.g. specific humidity at 400 hPa), and the subscript r the reference state variable (namely the results of the simulation by WRF). The summation is over all members of the state parameter in the spatial domain at the simulation time t. The overbar represents the mean value averaged for the spatial domain for the particular simulation time. The variation of the anomaly correlation coefficient is shown in Fig. 18.

This Fig. demonstrates the large correlation between the retrievals and the reference fields, which is encouraging. There appears a degradation of the correlation over time especially for moisture. This might be the result of the adopted training dataset, i.e. that it is not representative for the (t,q) values at a later stage of the simulation. This is to be expected as it is a simulation for the evolution of a severe convective situation. And the training dataset is taken from the pre-convective situation.

A retrieval simulation which excluded the radiometric noise in the synthetic radiances indicated that this noisy behaviour in the retrievals is largely induced by the noise in the
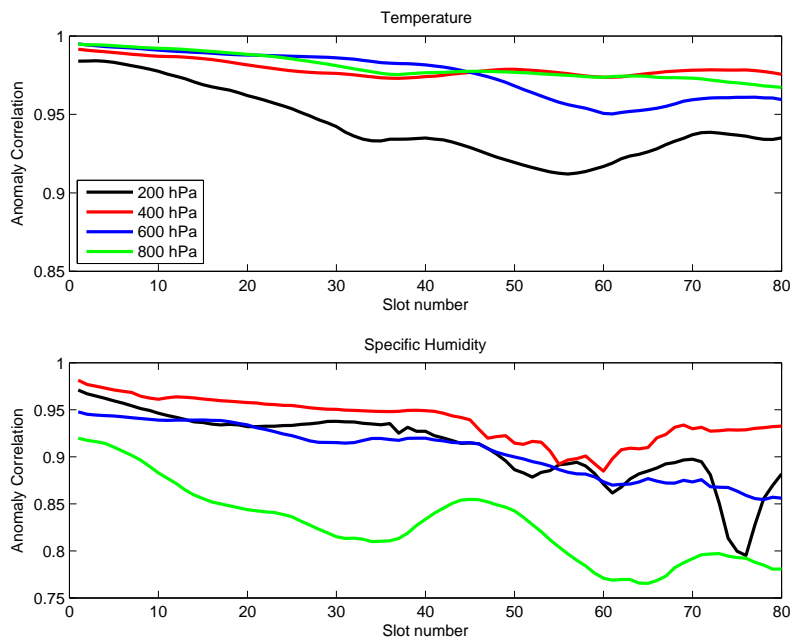
Figure 18 Variation of the anomaly correlation coefficient as a function of time for the retrieved temperature (top panel) at four different levels as indicated in the legend, and retrieved specific humidity (bottom panel).

spectrum. This suggests that the handling of radiometric noise should be considered with care, which is an opposite conclusion from the IC analysis discussed above.

Using the Optical Flow method, the retrieved moisture fields for 17:20 and 17:40 UTC were used to derive an atmospheric motion vector field which is shown in Fig. 21. This vector field should be compared to the Figures shown in the introduction (Fig. 2). Visual inspection of the Figs. indicate areas where the retrieved AMV field corresponds quite nicely to the modeled wind vector field, but that there are several areas where they diverge. These differences and agreements between the retrieved AMV and the modeled wind field will be part of future research.

Summary

The objective of the current work was to document the capabilities of the IRS candidate mission to meets its mission objective using the IRS phase A specifications to described the instrument performance. The initial results indicate the areas of concern like the potential bias in the retrieved moisture and temperature profiles induced by the pseudo-noise from nearby clouds. More work will be needed to further understand the capabilities of the candidate mission, especially how the instrument characteristics influences the depiction of atmospheric motion.
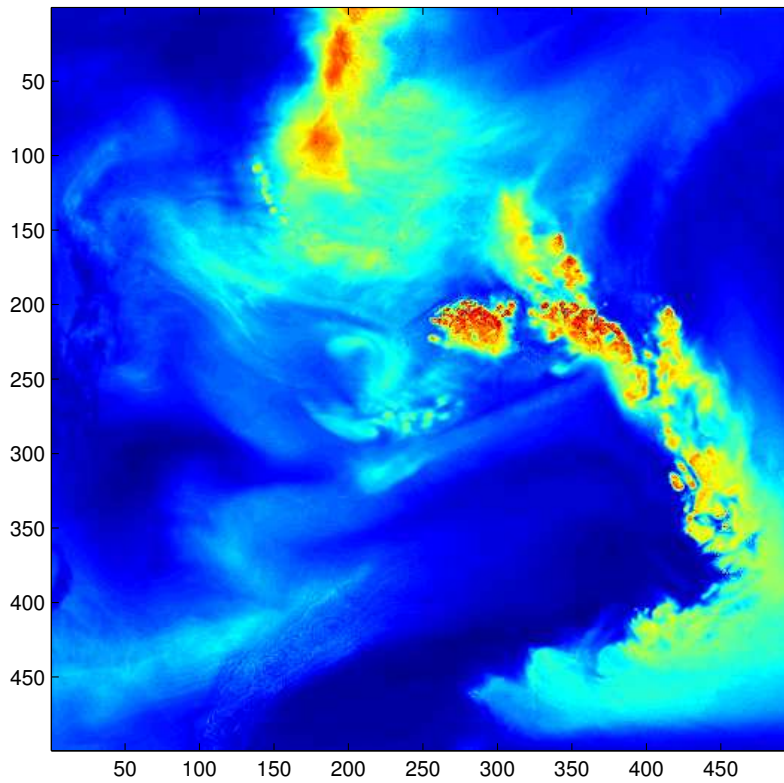
Figure 19 Same as Fig. 15, but now for a retrieval which does not consider radiometric noise in the synthetic radiances.

References

Corpetti T., E. Mémin and P. Pérez (2002). Dense estimation of fluid flows. IEEE Trans. Pattern Analysis Machine Intelligence, 24, 3, pp 365-380. Horn B. K. P. and B. G. Schunck (1981) Determining optical flow. Artificial Intelligence, 17, pp 185-203.

Szantai A. and F. Désalmand (2004) Using multiple channels from MSG to improve atmospheric motion wind selection and quality. Proc. 7th International Winds Workshop, Helsinki, Finland (14-17 June 2004). EUMETSAT EUM P 42, pp 307-314.

L. Zhou, C. Kambhamettu, and D. Goldgof. Fluid structure and motion analysis from multi-spectrum 2D cloud images sequences. In Proc. Conf. Comp. Vision Pattern Rec., volume 2, pages 744-751, Hilton Head Island, South Carolina, USA, 2000.

Li, J., W.W. Wolf, W.P. Menzel, W. Zhang, H.L. Huang and T.H Achtor, 2000: Global soundings of the atmosphere from ATOVS measurements: The Algorithm and Validation. J. Appl. Meteor., **39**, 1248 – 1268.

Clough S.A., M.W. Shephard, E.J. Mlawer, J.S. Delamere, M.J. Iacono, K. Cady-Pereira, S. Boukabara, P.D. Brown: Atmospheric radiative transfer modeling: A summary of the AER codes. J.Q.R.S.T 2004.

Huang, X.Y, Y.H Kuo and J. Done, 2005: Potential of Meteosat Third Generation to detect water vapour convergence linked to severe convection. Final report EUM/PPS/SOW/02/0089 available from www.eumetsat.int.
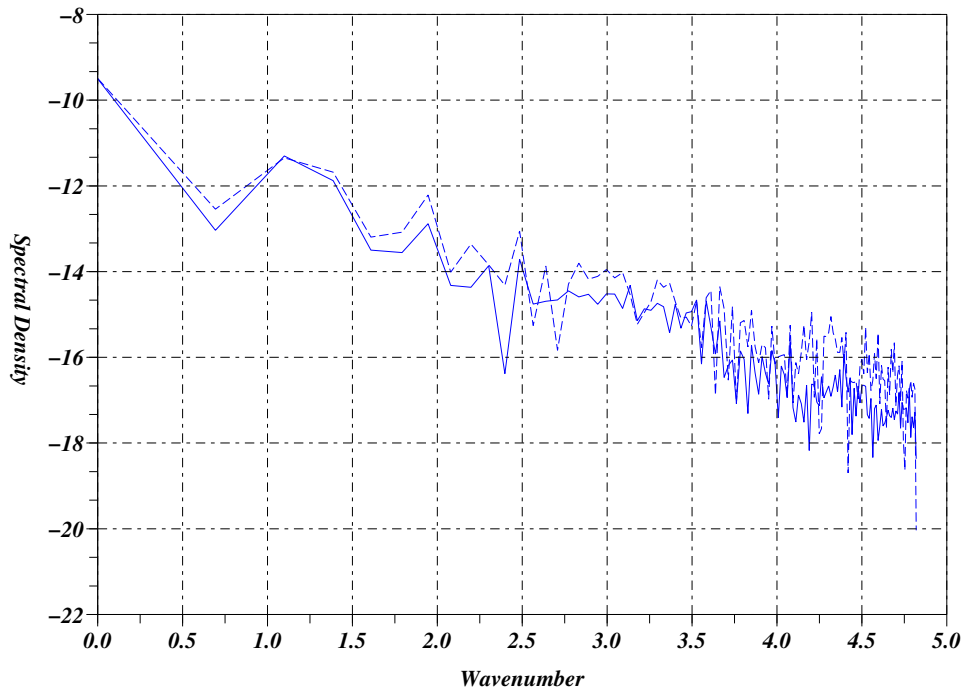
Figure 20 Same as Fig. 17, but now for a retrieval which does not consider radiometric noise in the synthetic radiances.
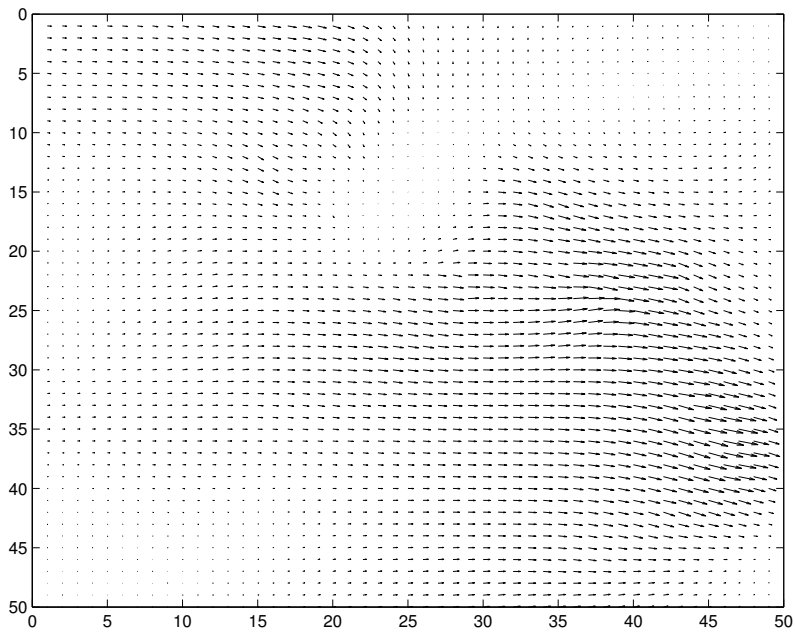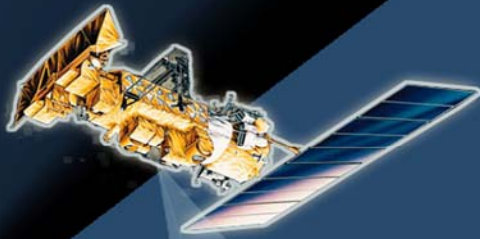
Figure 21 Atmospheric motion vectors derived from the retrieved moisture fields for 17:20 and 17:40 UTC. Retieval considers radiometric noise in the synthetic observations.

INTERNATIONAL
A TOVS
WORKING GROUP

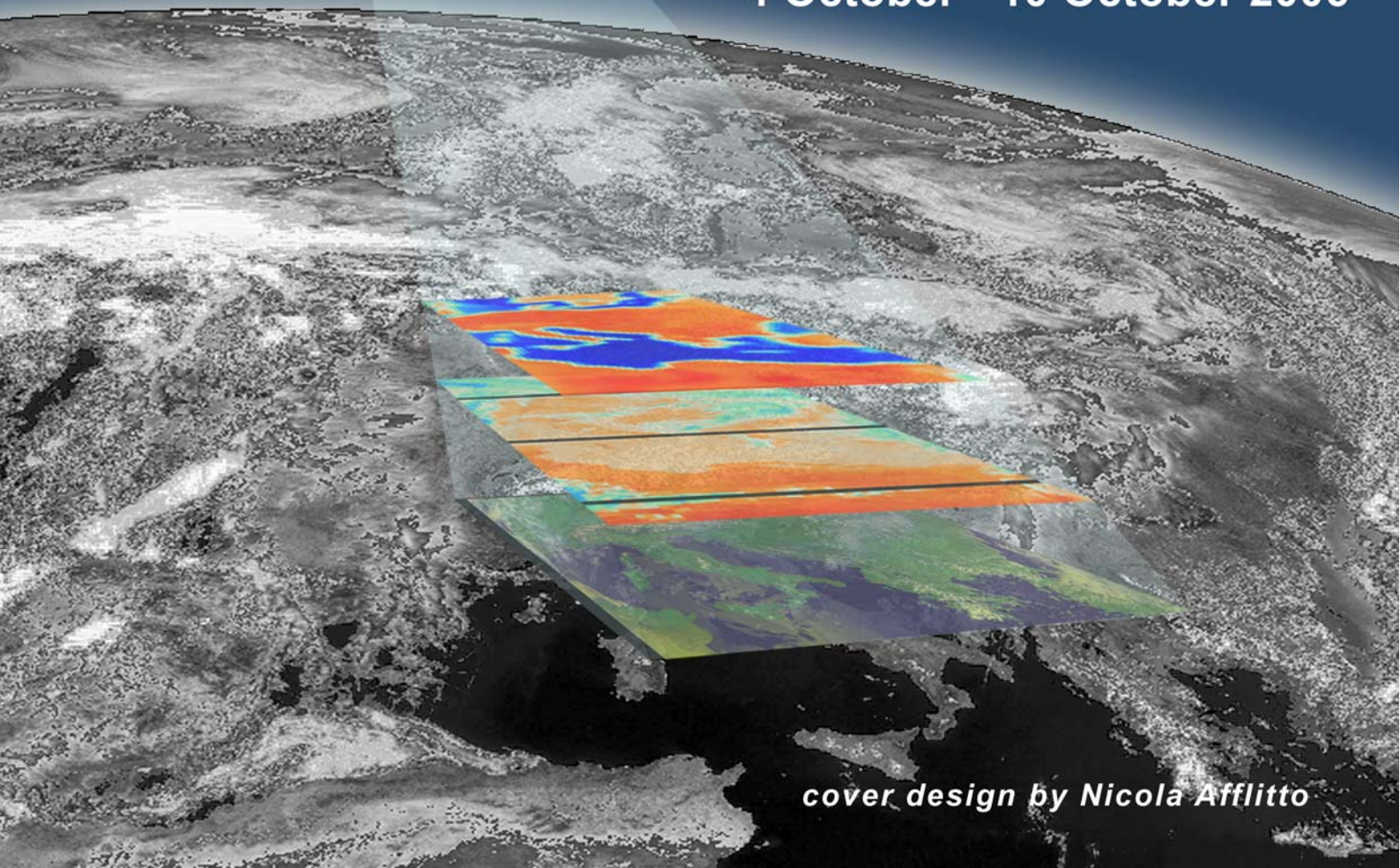*Sharing ideas, plans and techniques*

to study the earth's weather

using space-based observations

Proceedings of the

Fifteenth International

TOVS Study Conference

Maratea, Italy

4 October - 10 October 2006

cover design by Nicola Afflitto